

Cgsm Reference Manual: An Overture Solver for the Solving the Equations of Solid Mechanics,

William D. Henshaw

Department of Mathematical Sciences,
Rensselaer Polytechnic Institute,
Troy, NY, 12180,
www.overtureframework.org

June 13, 2014

Abstract:

This is the reference guide for **Cgsm**. Cgsm is a program that can be used to solve the elastic wave equation and other equations of solid mechanics in two and three dimensions using composite overlapping grids. It is built upon the **Overture** object-oriented framework. This reference guide describes in some detail the equations being solved, the discrete approximations, time-stepping methods, boundary conditions and convergence results. The reference guide also contains various notes related to different aspects of the equations. The reference guide concludes by providing a collection of interesting computations that have been performed with Cgsm.

Contents

1	Introduction	3
2	Governing equations	3
3	Sample Simulations	5
3.1	Vibrational modes of an elastic sphere	5
3.2	Diffraction of a p-wave “shock” by a circular cavity	7
3.3	Vibrating Beam	11
3.3.1	Beam theories	11

1 Introduction

This is the reference guide for **Cgsm**. Cgsm is a program that can be used to solve the elastic wave equation and other equations of solid mechanics in two and three dimensions using composite overlapping grids. It is built upon the **Overture** object-oriented framework [2],[5],[3]. This reference guide describes in some detail the equations being solved, the discrete approximations, time-stepping methods, boundary conditions and convergence results. The reference guide also contains various notes related to different aspects of the equations. The reference guide concludes by providing a collection of interesting computations that have been performed with Cgsm.

2 Governing equations

Consider an elastic solid that at time $t = 0$ occupies the domain $\Omega \subset \mathbb{R}^{n_d}$ in $n_d = 2$ or $n_d = 3$ space dimensions. Let $\mathbf{u}(\mathbf{x}, t)$, with components $u_i(\mathbf{x}, t)$, denote the displacement of a material particle originally located at position $\mathbf{x} \in \mathbb{R}^{n_d}$, and let $\boldsymbol{\sigma}(\mathbf{x}, t)$ denote the Cauchy stress tensor with components $\sigma_{ij}(\mathbf{x}, t)$. It is assumed that the solid is a homogeneous isotropic material, and that the evolution of the displacement is governed by the equations of linear elasticity given by (with Einstein summation convention),

$$\rho \frac{\partial^2 u_i}{\partial t^2} = \frac{\partial \sigma_{ij}}{\partial x_j} + \rho f_i, \quad \mathbf{x} \in \Omega, \quad t > 0, \quad i = 1, 2, \dots, n_d, \quad (1)$$

where ρ is the density of the material (taken to be constant), \mathbf{f} is an acceleration due to an applied body force, and the components of stress are given by

$$\sigma_{ij} = \lambda (\epsilon_{kk}) \delta_{ij} + 2\mu \epsilon_{ij}, \quad \epsilon_{ij} = \frac{1}{2} \left(\frac{\partial u_i}{\partial x_j} + \frac{\partial u_j}{\partial x_i} \right). \quad (2)$$

Here, ϵ_{ij} and δ_{ij} are the components of the (linear) strain tensor and the identity tensor, respectively, $\epsilon_{kk} = \sum_k \epsilon_{kk} = \nabla \cdot \mathbf{u}$ is the divergence of the displacement, and λ and μ are Lamé parameters. The latter are related to Young's modulus E and Poisson's ratio ν by $\mu = E/(2(1 + \nu))$, and $\lambda = \nu E/((1 + \nu)(1 - 2\nu))$. Initial conditions for the second-order system in (1) are

$$\mathbf{u}(\mathbf{x}, 0) = \mathbf{u}_0(\mathbf{x}), \quad \frac{\partial \mathbf{u}}{\partial t}(\mathbf{x}, 0) = \mathbf{v}_0(\mathbf{x}), \quad \mathbf{x} \in \Omega, \quad (3)$$

where $\mathbf{u}_0(\mathbf{x})$ and $\mathbf{v}_0(\mathbf{x})$ are the initial displacement and velocity of the solid, respectively. Boundary conditions for (1) are applied for $\mathbf{x} \in \partial\Omega$ and take various forms. The available boundary conditions are

$$\mathbf{u} = \mathbf{g}_d(\mathbf{x}, t), \quad \text{displacement boundary condition,} \quad (4)$$

$$\mathbf{n} \cdot \boldsymbol{\sigma} = \mathbf{g}_t(\mathbf{x}, t), \quad \text{traction boundary condition,} \quad (5)$$

$$\left. \begin{array}{l} \mathbf{n} \cdot \mathbf{u} = g_s(\mathbf{x}, t) \\ \mathbf{n} \cdot \boldsymbol{\sigma} \cdot \boldsymbol{\tau}_\alpha = g_{s,\alpha}(\mathbf{x}, t) \end{array} \right\} \quad \text{slip-wall boundary conditions.} \quad (6)$$

Here, \mathbf{n} is the unit outward normal on the boundary and $\boldsymbol{\tau}_\alpha$, $\alpha = 1, \dots, n_d - 1$, are unit tangent vectors (assumed to be mutually orthogonal). The functions $\mathbf{g}_d(\mathbf{x}, t)$ and $\mathbf{g}_t(\mathbf{x}, t)$ give the displacement and traction at the boundary, respectively, while $g_s(\mathbf{x}, t)$ and $g_{s,\alpha}(\mathbf{x}, t)$ define the slip wall motion. The elastic wave equation (1)-(2) with initial conditions (3) and boundary conditions (4)-(6) is a well-posed problem, see, for example [4].

We also consider the equations in (1) and (2) written as a first-order system

$$\left. \begin{array}{l} \frac{\partial u_i}{\partial t} = v_i, \\ \frac{\partial v_i}{\partial t} = \frac{1}{\rho} \frac{\partial \sigma_{ij}}{\partial x_j} + f_i, \\ \frac{\partial \sigma_{ij}}{\partial t} = \lambda (\dot{\epsilon}_{kk}) \delta_{ij} + 2\mu \dot{\epsilon}_{ij}, \end{array} \right\} \quad \mathbf{x} \in \Omega, \quad t > 0, \quad i = 1, 2, \dots, n_d, \quad (7)$$

where $\mathbf{v}(\mathbf{x}, t)$, with components $v_i(\mathbf{x}, t)$, is the velocity and the components $\dot{\epsilon}_{ij}$ of the rate of strain tensor are given by

$$\dot{\epsilon}_{ij} = \frac{1}{2} \left(\frac{\partial v_i}{\partial x_j} + \frac{\partial v_j}{\partial x_i} \right).$$

Initial conditions for displacement and velocity are given by $\mathbf{u}_0(\mathbf{x})$ and $\mathbf{v}_0(\mathbf{x})$ as before, and initial conditions for the components of stress may be derived from (2) applied at $t = 0$. Boundary conditions for the first-order system may be taken directly from those described in (4), (5) and (6) for the second-order system. Note that contrary to what is typically done, we retain the displacements in our formulation of the first order system. The displacements are coupled with the velocity and stress through the boundary conditions as discussed in Section ???. Retaining the displacements in the formulation allows the stress-strain relationship (2) to be explicitly imposed at the boundary. In addition it will be useful to have the displacement field when solving fluid-structure interaction problems (to define the fluid-solid interface for grid generation, for example).

The governing equations, whether written as a second-order or first-order system, are hyperbolic and represent the motion of elastic waves in the solid. For the second-order system, the characteristic wave speeds are $\pm c_p$ and $\pm c_s$, where the pressure and shear wave speeds are given by

$$c_p = \sqrt{\frac{\lambda + 2\mu}{\rho}}, \quad c_s = \sqrt{\frac{\mu}{\rho}}. \quad (8)$$

The first-order system has the wave speeds above as well as characteristics speeds equal to zero.

3 Sample Simulations

3.1 Vibrational modes of an elastic sphere

In this section, we consider small amplitude vibrations of a solid elastic sphere. This is a classical problem in linear elasticity, and exact solutions are discussed in Lamb [7] and Love [8], for example. Solutions of the linear problem are expressed as a sum of vibrational modes, and we consider one such mode (a so-called solution of the *second class*) for the purpose of verification of our numerical methods. For a sphere of radius R , the j^{th} component of displacement of the n^{th} mode in Cartesian coordinates (x_1, x_2, x_3) can be written in the form

$$u_j^{(n)} = A_n \cos(\omega_n t) \left\{ -\frac{1}{\alpha_n^2} \left(\frac{\partial \zeta_n}{\partial x_j} \right) \psi_n(\alpha_n \varrho) - (x_j \zeta_n) \psi_{n+1}(\alpha_n \varrho) + C_n \left[\frac{1}{\kappa_n^2} \left(\frac{\partial \zeta_n}{\partial x_j} \right) \psi_{n-1}(\kappa_n \varrho) - \frac{n}{n+1} \left(r^2 \frac{\partial \zeta_n}{\partial x_j} - (2n+1) x_j \zeta_n \right) \psi_{n+1}(\kappa_n \varrho) \right] \right\}, \quad (9)$$

where A_n is the amplitude of the mode, ω_n is its frequency, α_n and κ_n are constants related to the frequency by

$$\alpha_n^2 = \frac{\rho \omega_n^2}{\lambda + 2\mu}, \quad \kappa_n^2 = \frac{\rho \omega_n^2}{\mu}, \quad (10)$$

C_n is a constant, and ψ_n and ζ_n are functions given by

$$\psi_n(\varrho) = \left(\frac{1}{\varrho} \frac{d}{d\varrho} \right)^n \left(\frac{\sin \varrho}{\varrho} \right), \quad \zeta_n(\varrho, \theta, \phi) = \varrho^n e^{im\theta} P_n^m(\cos \phi). \quad (11)$$

Here, ψ_n is related to the spherical Bessel function (of the first kind) of order n , ζ_n is the solid spherical harmonic of order n , and P_n^m is the associated Legendre function of order n and degree m . These functions are written in terms of the usual spherical polar coordinates (ϱ, θ, ϕ) , where $0 \leq \varrho \leq R$, $0 \leq \theta \leq 2\pi$, and $0 \leq \phi \leq \pi$ for the solid sphere. Application of a stress-free boundary condition at $r = R$ provides constraints that determine an infinite number of (κ_n, C_n) pairs for each n (independent of m), see [8]. Corresponding values for α_n and ω_n may then be found using (10).

Within the class of solutions given in (9), we consider the mode $n = 2$ with $m = 0$, i.e. spheroidal vibrations. For this case, the solid spherical harmonic function in (11) becomes independent of θ , and it takes the simple form

$$\zeta_2 = \frac{\varrho^2}{2} (3 \cos^2 \phi - 1) = x_3^2 - \frac{1}{2} (x_1^2 + x_2^2), \quad (12)$$

using $\varrho^2 = x_1^2 + x_2^2 + x_3^2$ and $\cos \phi = x_3/\varrho$. The formula for the solid spherical harmonic in (12) may now be used in (9) to give the solution mode

$$u_j^{(2)} = A_2 \cos(\omega_2 t) \hat{u}_j^{(2)}, \quad j = 1, 2, 3, \quad (13)$$

where

$$\hat{u}_j^{(2)} = x_j \left\{ \frac{1}{\alpha_2^2} \psi_2(\alpha_2 \varrho) - \frac{1}{2} (2x_3^2 - r^2) \psi_3(\alpha_2 \varrho) - C_2 \left[\frac{1}{\kappa_2^2} \psi_1(\kappa_2 \varrho) + \frac{1}{3} (8x_3^2 - 7r^2) \psi_3(\kappa_2 \varrho) \right] \right\},$$

for $j = 1$ and 2 , and

$$\hat{u}_3^{(2)} = -x_3 \left\{ \frac{2}{\alpha_2^2} \psi_2(\alpha_2 \varrho) + \frac{1}{2} (2x_3^2 - r^2) \psi_3(\alpha_2 \varrho) - C_2 \left[\frac{2}{\kappa_2^2} \psi_1(\kappa_2 \varrho) + \frac{1}{3} (6x_3^2 - 7r^2) \psi_3(\kappa_2 \varrho) \right] \right\}.$$

Here, ψ_1 , ψ_2 and ψ_3 are given by the formula in (11) and $r^2 = x_1^2 + x_2^2$. Three values for (κ_2, C_2) , corresponding to the lowest three frequencies of vibration for this mode, are listed in Table 1 for the case

	$\kappa_2 R$	C_2
1	2.63986927790186	-2.61595562778538
2	4.86527284993742	-1.89108063594100
3	8.32919545905501	3.21915564815474

Table 1: Leading three values for (κ_2, C_2) for the vibration mode with $n = 2$ given in (13) for a sphere of radius R .

$\lambda = \mu$. The solution mode given by (13) is axisymmetric, and corresponds to a sphere which elongates and compresses periodically along the x_3 -axis.

Modes of vibration of a solid sphere may be computed numerically using the overlapping grid shown in Figure 1. The overlapping grid is defined by four component grids, three of which are curvilinear and define the spherical boundary as shown in the figure. The fourth component grid is a Cartesian grid which covers the interior core of the solid sphere and is not visible in the figure. Most of the boundary-fitted spherical shell is covered by a spherical-polar grid defined by

$$\begin{aligned} \mathcal{S}([\varrho_a, \varrho_b] \times [\theta_a, \theta_b] \times [\phi_a, \phi_b], N_1, N_2, N_3) = \{ & (\varrho_{i_1} \cos \theta_{i_2} \sin \phi_{i_3}, \varrho_{i_1} \sin \theta_{i_2} \sin \phi_{i_3}, \varrho_{i_1} \cos \phi_{i_3}) \mid \\ & \varrho_{i_1} = \varrho_a + i_1(\varrho_b - \varrho_a)/N_1, \theta_{i_2} = \theta_a + i_2(\theta_b - \theta_a)/N_2, \phi_{i_3} = \phi_a + i_3(\phi_b - \phi_a)/N_3, \\ & i_\alpha = 0, 1, \dots, N_\alpha, \alpha = 1, 2, 3\} . \end{aligned} \quad (14)$$

The parts of the spherical shell near the north and south poles are covered by orthographic patches defined in (??), and the Cartesian grid in the interior is defined by the box grid in (??). The overlapping grid for the solid sphere of radius R , with resolution factor j , is given by

$$\begin{aligned} \mathcal{G}_{ss}^{(j)} = \mathcal{B}([-x_a, x_a]^3, N_x(j), N_x(j), N_x(j)) \cup \mathcal{S}([.75R, R] \times [0, 2\pi] \times [.2\pi, .8\pi], N_r(j), N_\theta(j), N_\phi(j)) \\ \cup \mathcal{O}_{\pm 1}([.75R, R], S_a, S_a, N_r(j), N_0(j), N_0(j)), \end{aligned}$$

where

$$\begin{aligned} x_a = .75R + 1.5h_j, \quad N_x(j) = \lfloor 2x_a/h_j \rfloor, \quad S_a = .65 + h_j/R, \quad N_0(j) = \lfloor .49S_a\pi R/h_j + 1.5 \rfloor, \\ N_r(j) = \lfloor .25R/h_j + 1.5 \rfloor, \quad N_\theta(j) = \lfloor 1.4\pi R/h_j + 1.5 \rfloor, \quad N_\phi(j) = \lfloor .51R\pi/h_j + 1.5 \rfloor, \end{aligned}$$

for a mesh spacing $h_j = R/(10j)$. Using the exact solution with the first (κ_2, C_2) pair in Table 1 to obtain initial conditions, numerical solutions are computed using the SOS and FOS schemes for the case $\rho = \lambda = \mu = 1$, $R = 1$ and $A_2 = 100$. (The amplitude is chosen so that the maximum displacement is about 1 in magnitude.) The deformation of the sphere is shown in Figure 1 for $t = 0, 0.8$ and 1.2 , and the maximum error between the various components of the numerical solution and the exact solution at $t = 0.5$ is given in Table 2 for four grid resolutions. The computed rates given in the table indicate that the numerical solutions given by the two schemes are both converging at a rate approximately equal to 2.

		SOS		FOS						
Grid	$\mathcal{G}^{(j)}$	h_j	$e_u^{(j)}$	r	$e_u^{(j)}$	r	$e_v^{(j)}$	r	$e_\sigma^{(j)}$	r
	$\mathcal{G}_{ss}^{(1)}$	1/10	1.3×10^{-1}		5.1×10^{-2}		1.2×10^{-1}		2.6×10^{-1}	
	$\mathcal{G}_{ss}^{(2)}$	1/20	4.0×10^{-2}	3.2	1.2×10^{-2}	4.2	3.0×10^{-2}	4.0	5.1×10^{-2}	5.1
	$\mathcal{G}_{ss}^{(4)}$	1/40	10.0×10^{-3}	4.0	2.4×10^{-3}	5.1	7.1×10^{-3}	4.2	8.6×10^{-3}	6.0
	$\mathcal{G}_{ss}^{(8)}$	1/80	2.4×10^{-3}	4.1	5.2×10^{-4}	4.6	1.7×10^{-3}	4.1	2.0×10^{-3}	4.3
rate			1.93		2.22		2.03		2.37	

Table 2: Maximum errors and estimated convergence rates for numerical solutions of a vibrational mode of a solid sphere using the SOS and FOS schemes.

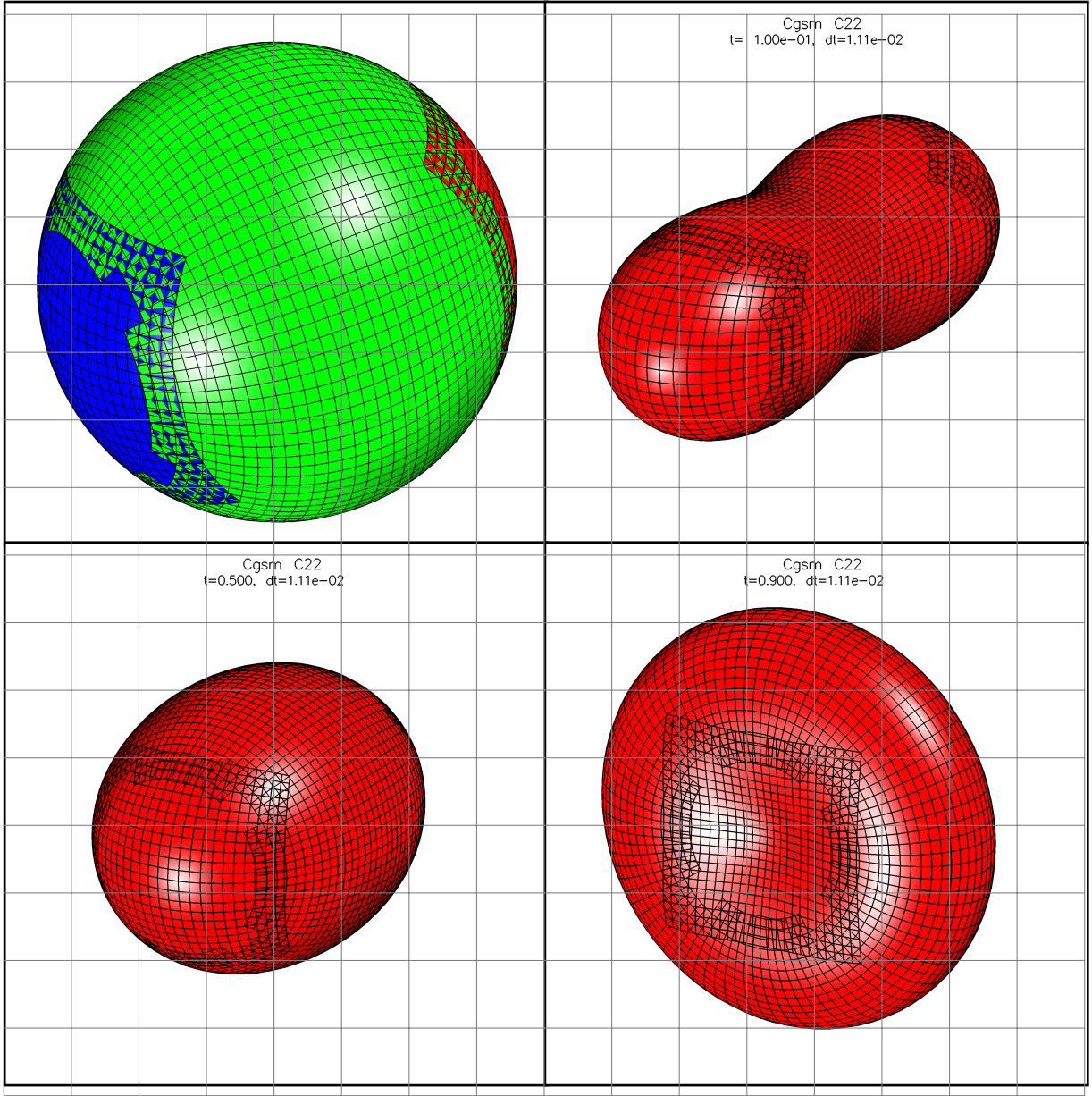


Figure 1: Vibrational mode of an elastic sphere. Left: overlapping grid for a solid sphere consisting of two orthographic patches, a spherical polar shell and an interior Cartesian grid (not visible). Middle to right: the deformed sphere at times $t = 0$, $t = 0.8$ and $t = 1.2$ for the case $\rho = \lambda = \mu = 1$ and $R = 1$. The displacement is scaled by a factor of 0.08 for illustrative purposes.

3.2 Diffraction of a p-wave “shock” by a circular cavity

To illustrate the use of adaptive mesh refinement we consider the diffraction of a p-wave “shock” by a circular cavity. The domain for this problem is taken to be the two-dimensional region interior to the square $[-3, 3]^2$ and exterior to the circle of radius $R = 0.5$. The initial conditions are taken from the exact traveling-wave solution for a planar p-wave with a piecewise constant velocity profile. The displacement and velocity for this solution are given by

$$\mathbf{u}(\xi) = \begin{cases} -\xi(v_0/c_p)\boldsymbol{\kappa} & \text{for } \xi < 0, \\ 0 & \text{for } \xi > 0, \end{cases} \quad \mathbf{v}(\xi) = \begin{cases} v_0 \boldsymbol{\kappa} & \text{for } \xi < 0, \\ 0 & \text{for } \xi > 0, \end{cases}$$

where

$$\xi = \boldsymbol{\kappa} \cdot (\mathbf{x} - \mathbf{x}_0) - c_p t, \quad c_p = \sqrt{(\lambda + 2\mu)/\rho}.$$

Here, $\boldsymbol{\kappa}$ defines the direction of propagation of the planar wave and \mathbf{x}_0 defines its position at $t = 0$. For the computations presented, we take $\boldsymbol{\kappa} = (1, 0)$, $v_0 = c_p$ and $\mathbf{x}_0 = (-1.25, 0)$, and we assume that $\rho = \lambda = \mu = 1$. The boundary conditions on the bottom and top sides of the square are slip-wall conditions, and exact data from the planar p-wave solution is used as Dirichlet conditions on the left and right sides of the square. A homogeneous traction condition is applied on the boundary of the circular cavity.

Calculations are performed using the SOS and FOS schemes with one level of AMR grids using a refinement factor of $n_r = 2$ or 4. The base-level composite grid for the two-dimensional domain is composed of a rectangular Cartesian grid defined previously in (??) and an annular grid defined in (??). This circle-in-a-square grid is defined by

$$\mathcal{G}_{CS}^{(j)} = \mathcal{R}([-3, 3]^2, N_x(j), N_x(j)) \cup \mathcal{C}([R, R + 7h_j], N_\theta(j), N_r),$$

where $h_j = 1/(10j)$ gives the approximate grid spacing, and the number of grid cells in the various coordinate directions are given by

$$N_x(j) = \lfloor 6/h_j + 1.5 \rfloor, \quad N_\theta(j) = \lfloor 2\pi(R + 3.5h_j)/h_j + 1.5 \rfloor, \quad N_r = 7.$$

We note that the composite grid uses a boundary-fitted annular grid with a fixed number of grid cells in the radial direction which is similar to the “narrow” grid, $\mathcal{G}_{Dn}^{(j)}$, used in Section ??.

Figure 2 shows the elastic response of the planar p-wave as it is diffracted by the circular cavity. The numerical solution is computed using the FOS scheme with the base-level composite grid given by $\mathcal{G}_{CS}^{(8)}$ and the addition of one refinement level with $n_r = 4$. The plots show shaded contours of the magnitude of velocity at times $t = 0, 1.0$ and 1.6 . When the p-wave meets the cavity, the boundary of the cavity is deformed and a reflected wave is created. The reflected wave consists of both pressure and shear waves which travel at different velocities as seen clearly in the plot at $t = 1.0$. The cavity continues to deform as the diffracted waves travel around it, and ultimately the waves collide near the back of the cavity as seen in the plot at $t = 1.6$. The behavior of the refinement grids are shown in the figure, and these grids are well-positioned during the calculation to increase the grid resolution of the various waves as they move in time throughout the domain.

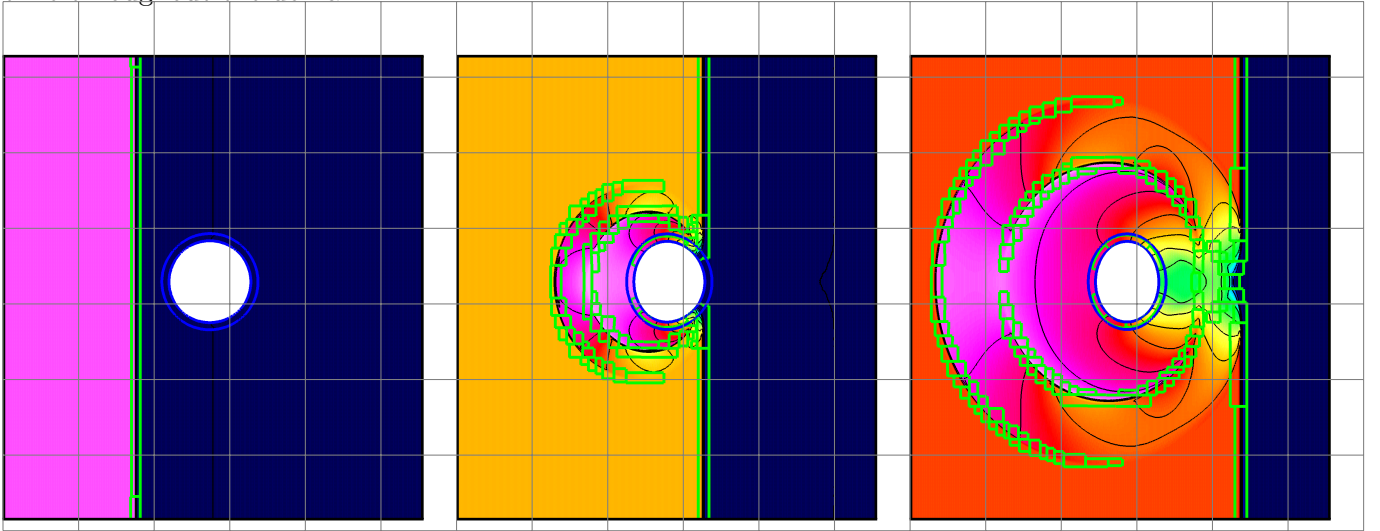


Figure 2: Diffraction of a p-wave shock by a circular cavity. Numerical solution computed with AMR using one refinement level with $n_r = 4$ and the FOS scheme. Shaded contours of the magnitude of velocity at times (from left to right) $t = 0$ (contour bounds $[0, 1.82]$), $t = 1.0$ ($[0, 2.79]$) and $t = 1.6$ ($[0, 2.41]$). The boundaries of the base-level component grids are shown in blue and the boundaries of the refinement grids are shown in green. The deformed grid is shown using a scaling of the displacement by a factor of 0.075.

Figure 3 compares the results for the SOS and FOS schemes for an AMR computation. For this comparison, we use the base grid $\mathcal{G}^{(8)}$ together with one level of $n_r = 4$ refinement. The magnitudes of

the displacement and velocity at time $t = 1.6$ are shown. From the figures it can be seen that the results from both schemes are generally in good agreement. The FOS results are less noisy than the SOS results, particularly in $|\mathbf{v}|$, which might be expected from the FOS approach as it is an upwinding scheme. Note, however, that the velocity is directly computed by FOS while for the SOS scheme it is computed in a post-processing step by a finite difference approximation in time, $\mathbf{v}_i^n = (\mathbf{u}_i^n - \mathbf{u}_i^{n-1})/\Delta t$, and this may contribute to some of the noise.

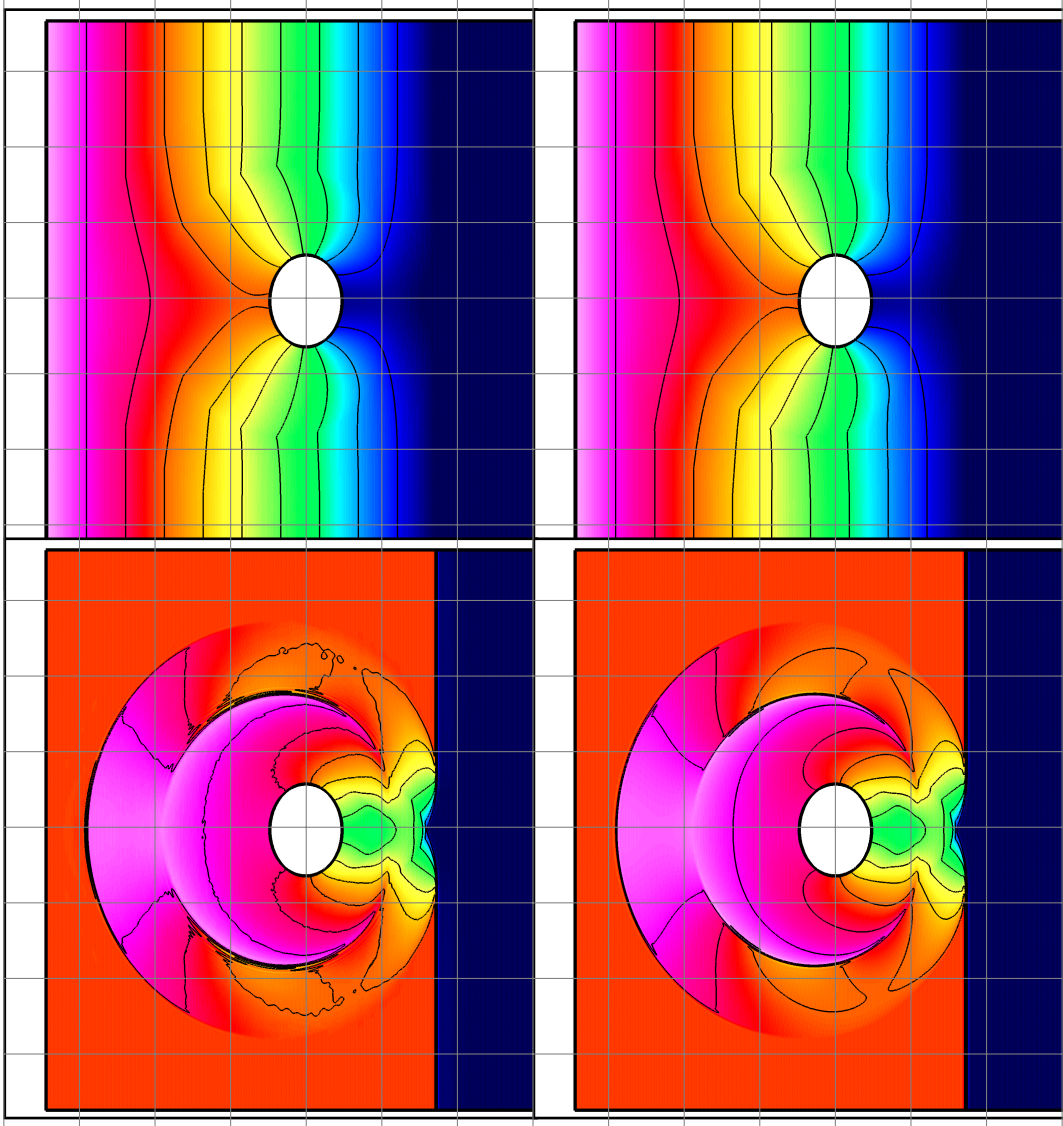


Figure 3: Diffraction of a traveling p-wave “shock” by a circular cavity at time $t = 1.6$ showing the norms of the displacement and velocity for the SOS scheme (left column) and FOS scheme (right column). Results are for the base grid $\mathcal{G}^{(8)}$ using one refinement level with $n_r = 4$. The contours are plotted on the deformed grid, scaling the displacement by a factor of 0.075.

The accuracy of the AMR computations for this example can be made more quantitative. Given a sequence of three grids of increasing resolution, a posteriori estimates of the errors and convergence rates can be computed using the procedure described in [6]. These self-convergence estimates assume that the numerical results are converging to some limiting solution. A posteriori estimates computed in this way are given in Table 3 for three grids of increasing resolution. The coarse grid computation used the base grid $\mathcal{G}_{CS}^{(2)}$ together with one refinement level of factor 2. The medium resolution computation used the base grid $\mathcal{G}_{CS}^{(2)}$ together with one refinement level of factor 4, while the finest resolution used the grid $\mathcal{G}_{CS}^{(64)}$ with

no AMR. The parameters in the AMR error estimate (??) were chosen as $c_1 = 0$, $c_2 = 1$ and $s_k = 1$. The error tolerances for the SOS scheme were taken as 4×10^{-3} and 1×10^{-3} for the coarse and medium resolutions respectively. The corresponding error tolerances for the FOS scheme were 10^{-2} and 2.5×10^{-3} respectively.

The table provides estimates of the L_1 -norm errors. Since the exact solution for the displacement has discontinuous first derivatives, one cannot expect second-order accurate convergence. We expect that the L_1 -norm error in the displacement would converge at rate of 1 in the limit of small h , while the errors in velocity and stress would converge at a rate of $2/3$, see [1]. The results in the table indicate that the computed convergence rates are close to the expected rates.

				SOS		FOS					
Grid	levels	n_r	h_j	$e_u^{(j)}$	r	$e_u^{(j)}$	r	$e_v^{(j)}$	r	$e_\sigma^{(j)}$	r
$\mathcal{G}_{CS}^{(2)}$	2	2	1/40	8.9×10^{-4}		2.1×10^{-3}		1.0×10^{-2}		1.2×10^{-2}	
$\mathcal{G}_{CS}^{(2)}$	2	4	1/80	4.7×10^{-4}	1.9	1.0×10^{-3}	2.0	6.4×10^{-3}	1.6	7.2×10^{-3}	1.6
$\mathcal{G}_{CS}^{(64)}$	—	—	1/640	7.1×10^{-5}	6.7	1.2×10^{-4}	8.5	1.5×10^{-3}	4.3	1.7×10^{-3}	4.3
rate				0.91		1.03		0.70		0.71	

Table 3: A posteriori estimated errors (L_1 -norm) and convergence rates at $t = 1.0$ for diffraction of a p-wave “shock” by a circular cavity using AMR. Note that the finest grid is a factor 8 times finer than the previous resolution.

3.3 Vibrating Beam

A beam can be modeled using the bulk Cgsm solvers. The results can be compared to the Euler-Bernoulli beam theory. See `cg/sm/runs/beam`.

A standing wave solution to the Euler-Bernoulli beam equation is

$$y(x) = a \sin(kx) \sin(\omega t),$$

where the frequency of vibration of an Euler-Bernoulli beam is

$$\omega = \sqrt{\frac{EI k^4}{\rho b h}}$$

We take

$$\rho = \lambda = \mu = 1, \rightarrow \nu = \frac{\lambda}{2(\lambda + \mu)} = \frac{1}{4}, \quad E = 2\mu(1 + \nu) = \frac{5}{2},$$

$$\frac{I}{b} = \frac{h^3}{12}.$$

For

$$h = .04 \quad T = \frac{2\pi}{\omega} \approx 17.43,$$

$$h = .02 \quad T = \frac{2\pi}{\omega} \approx 8.717$$

Figure 4 shows results from a calculation for $h = .04$ and $k = 2\pi$. Note that the *fibers* (lies normal to the neutral axis of the beam) remain nearly straight, of constant length and perpendicular to the neutral axis. These are consistent with the assumptions of Euler-Bernoulli beam theory. The approximate period of vibrartion is $T = 8.7$ which agrees well with the Euler-Bernoulli beam theory.

3.3.1 Beam theories

Here are some notes on beam theories.

Ref. Graff.

Euler-Bernoulli beam (small deflections, low frequency response)

$$\rho A \partial_t^2 y + \partial_x^2 (EI \partial_x^2 y) = q(x, t)$$

Large rotation Euler-Bernoulli beam (using the von Karman strains, ref. wikipedia)

$$\rho A \partial_t^2 y + \partial_x^2 (EI \partial_x^2 y) - \frac{3}{2} EA (\partial_x y)^2 \partial_x^2 y = q(x, y)$$

Timoshenko beam theory (accounts for shearing effects, high frequency response)

$$\rho A \partial_t^2 y + GA \kappa (\partial_x \psi - \partial_x^2 y) = q(x, y)$$

$$\rho I \partial_t^2 \psi + GA \kappa (\psi - \partial_x y) - EI \partial_x^2 \psi = q(x, y)$$

or upon eliminating ψ

$$\frac{EI}{\rho A} \partial_x^4 y - \frac{I}{A} \left(1 + \frac{E}{G \kappa}\right) \partial_x^2 \partial_t^2 y + \partial_t^2 y + \frac{\rho I}{GA \kappa} \partial_t^4 y = \dots$$

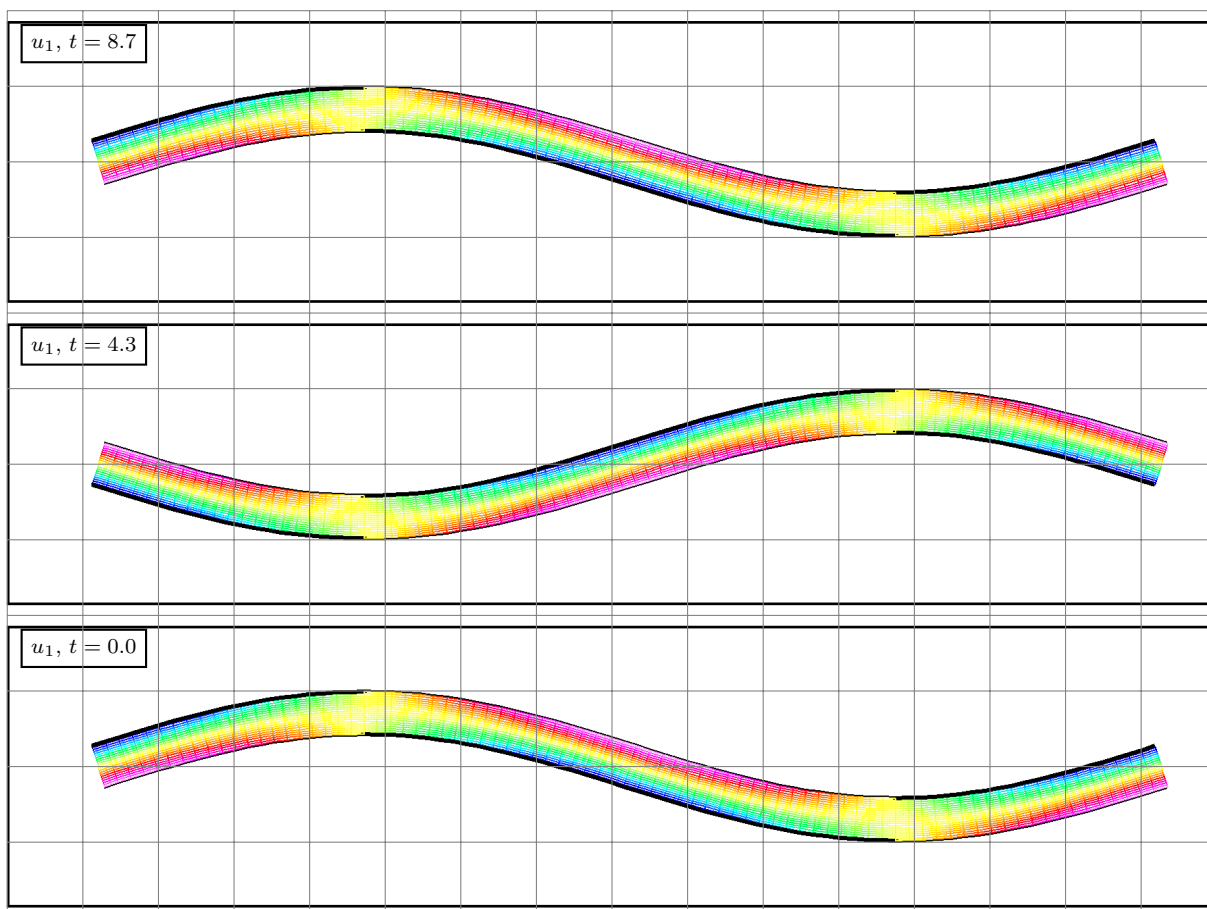


Figure 4: Vibrating beam simulated using the bulk solid solvers.

References

- [1] J. W. BANKS, T. ASLAM, AND W. J. RIDER, *On sub-linear convergence for linearly degenerate waves in capturing schemes*, J. Comput. Phys., 227 (2008), pp. 6985–7002. [publications/BanksAslamRiderSubLinear2008.pdf](#).
- [2] D. L. BROWN, G. S. CHESHIRE, W. D. HENSHAW, AND D. J. QUINLAN, *Overture: An object oriented software system for solving partial differential equations in serial and parallel environments*, in Proceedings of the Eighth SIAM Conference on Parallel Processing for Scientific Computing, 1997, p. .
- [3] D. L. BROWN, W. D. HENSHAW, AND D. J. QUINLAN, *Overture: An object oriented framework for solving partial differential equations*, in Scientific Computing in Object-Oriented Parallel Environments, Springer Lecture Notes in Computer Science, 1343, 1997, pp. 177–194.
- [4] K. F. GRAFF, *Wave Motion in Elastic Solids*, Dover Publications, 1991.
- [5] W. D. HENSHAW, *Overture: An object-oriented system for solving PDEs in moving geometries on overlapping grids*, in First AFOSR Conference on Dynamic Motion CFD, June 1996, L. Sakell and D. D. Knight, eds., 1996, pp. 281–290.
- [6] W. D. HENSHAW AND D. W. SCHWENDEMAN, *Parallel computation of three-dimensional flows using overlapping grids with adaptive mesh refinement*, J. Comput. Phys., 227 (2008), pp. 7469–7502. [publications/henshawSchwendemanPOG2008.pdf](#).
- [7] H. LAMB, *On the vibrations of an elastic sphere*, Proceedings of the London Mathematical Society, 13 (1882), pp. 189–212.
- [8] A. E. H. LOVE, *A Treatise on the Mathematical Theory of Elasticity*, Dover Publications, New York, 1944.